

Breaking symmetry in propagation of radially and azimuthally polarized high power laser pulses in underdense plasma

Naveen Pathak^{1,2}, Alexei Zhidkov^{1,2}, Nobuhiko Nakanii^{1,2},
Shinichi Masuda^{1,2}, Tomonao Hosokai^{1,2}, R Kodama^{1,2,3,4}

¹ *Photon Pioneers Center, Osaka University, 2-1 Yamada-oka, Suita, Osaka 565-0871, Japan*

² *CREST, Japan Science and Technology Agency, 2-1 Yamada-oka, Suita, Osaka 565-0871, Japan*

³ *Graduate School of Engineering, Osaka University, 2-1 Yamada-oka, Suita, Osaka 565-0871, Japan*

⁴ *Institute of Laser Engineering, Osaka University, 2-8 Yamada-oka, Suita, Osaka 565-0871, Japan*

Abstract

Propagation of relativistically intense azimuthally or radially polarized laser pulses (RPP) in underdense plasmas is demonstrated to be unstable, via 3D particle-in-cell simulation and disregarding the Kerr non-linearity. Strong pulse filamentation occurs for RPP in transversely uniform plasma with an increment, Γ , close to the well-known one depending on acceleration, α , and modulated density gradient length, L , as $\Gamma \approx (\alpha/L)^{1/2}$. In deep plasma channels the instability vanishes. Electron self-injection and acceleration by the resulting laser pulse wake is explored.

1 Introduction

Stable and controlled propagation of high power laser pulses in underdense plasma is a crucial part of laser-driven plasma accelerators [1, 2, 3, 4], which are becoming important for high-temporal and spatial resolution imaging systems [5, 6, 7] as well as for the ultra-high energy multistage acceleration technique [8, 9]. There are two parts of the laser pulse propagation which have to be controlled for laser-driven acceleration: (i) formation of a pulse wake with required field distribution, and (ii) self-injection of plasma electrons in the acceleration phase of the wakefield [10]. Usually, Gaussian laser pulses are used for laser wakefield acceleration (LWFA). However, some laser modes can be useful for controlled electron self-injection and (or) further electron acceleration. Here, radially or azimuthally polarized laser pulses are of particular interest being two TEM01 or TEM10 modes, nearest to the Gaussian (TEM00) mode. Because of their strong longitudinal electric field at the focus, these modes at high pulse power have been proposed for direct electron acceleration [11, 12, 13]. In Ref. [14] the radially polarized laser pulses have been proposed theoretically for an efficient electron wakefield acceleration as well. In contrast, in experiments [15] the radially and azimuthally polarized laser pulses exhibited spectra of side scattered light very different from spectra for Gaussian laser pulses: there was no typical red shift (and/or blue shift) in Thomson scattering originating from plasma wave formation [16]. This may be a result of some kind of instability, and makes investigation of propagation of such laser pulses in plasma in the real geometry particularly important.

Instabilities are an inevitable part of the laser plasma interaction process, and play an important role in governing the interaction mechanism. There have been many different kinds of instabilities reported and investigated both theoretically and experimentally: Raman, Brilluion, modulation, filamentation instabilities, and so on [17, 18, 19]. The filamentation instability results in transverse disintegration of a laser pulse into several filaments. Periodic breakup of radially symmetrical optical beams due to self-focusing in a Kerr-type medium was first reported by Campillo et. al. [20]. Experimentally they

demonstrated that a radially symmetric Fresnel patterns break up into focal spots having azimuthal symmetry and regular spacing. Yankauskas et al. [21], have proposed that, for a medium with Kerr-type nonlinearity, an infinite number of bound states with cylindrical symmetry should exist, where, bound state implies a central bright spot surrounded by annular rings of varying dimension. Stability of cylindrically symmetric higher-bound states is investigated analytically and numerically by Soto-Crespo et. al. [22]. They found that higher-bound states are susceptible to the filamentation instability. A similar study was also carried out by Skryain et. al [23]. A common point in all these transverse beam break up studies is that they rely on the optical Kerr effect. However, in the propagation of an ultra-intense laser pulses over shorter distances, \sim few mm, the Kerr effect is not usually significant; the self-focusing of the laser pulses is governed by ponderomotive and (or) relativistic effects [24]. The ponderomotive and relativistic nonlinearities, along with the non-uniformity in the laser and plasma conditions, may result in the spatial-temporal break up of a laser beam into multiple arbitrary number of filaments. An extensive investigation of such a filamentation instability has been done both theoretically and numerically for linearly or circularly polarized laser pulses [25, 26], but no such filamentation instability was explored with radially or azimuthally polarized laser pulses, where the pulse transverse mode structure is different.

In this paper we examine the symmetry breaking instability when an intense radially or azimuthally polarized laser pulse propagates in uniform underdense plasmas, using 3D particle-in-cell simulation. This instability results in transverse breakup of the pulse into multiple filaments. The unique feature of this instability is that the filaments which appear are symmetric and non-randomized in space. Moreover, depending on the intensity of the laser pulse the number of filaments appear as an integral multiple of three. In the best of our knowledge, this is for the first time such a harmonic behaviour of filamentation instability is reported for radially polarized laser pulse. In simulations, it was found that this instability is triggered by the interaction of the radially or azimuthally polarized laser pulses with self-induced positive plasma density compression along the propagation axis.

However, in contrast to the Gaussian laser pulses, the relativistic self-focusing results in shrinking of the radially symmetrical laser pulse ring. In the reference frame moving with the laser pulse, the stability conditions resemble mathematically to the conditions for the Rayleigh-Taylor instability. The real geometry particle-in-cell simulation not only allows the conditions for instability and its increment to be studied, but the entire nonlinear process. To avoid misunderstanding in the nature of the instabilities, we exclude the Kerr non-linearity from our fully relativistic simulation.

2 Equilibrium conditions in laser pulse propagation

The dynamics of the interaction between the laser pulse and plasma density can be given in terms of the following equations:

$$mN_e \left[\frac{\partial \vec{v}_\perp}{\partial t} + (\vec{v}_\perp \cdot \vec{\nabla}) \vec{v}_\perp \right] = \frac{-e^2 N_e}{4\gamma m \omega_L^2} \vec{\nabla}_\perp \vec{A}^2 - eN_e \vec{\nabla}_\perp \varphi \quad (1)$$

$$\Delta \varphi = -4\pi e(N_0 - N_e) \quad (2)$$

$$\frac{\partial N_e}{\partial t} + \vec{\nabla} \cdot (\vec{v}_\perp N_e) = 0 \quad (3)$$

where m is the mass of electron, N_e is the electron density, N_0 is the non-perturbed ion density, \vec{A} is the vector potential and φ is the scalar potential, \vec{v}_\perp is the transverse velocity of plasma electrons, ω_L is the laser frequency, e is the electron charge and γ is the relativistic factor of the plasma electrons, $\gamma = \sqrt{1 + a_0^2/2}$ with $a_0 = eE_L/mc\omega_L$ and $\vec{E}_L = -\partial \vec{A}/\partial(ct)$. The vector potential is a solution of the well know equation

$$\Delta \vec{A} - \frac{\partial^2 \vec{A}}{c^2 \partial t^2} = -\frac{\partial \vec{\nabla} \varphi}{c^2 \partial t} - \frac{4\pi \vec{j}}{c} \quad (4)$$

and

$$\vec{\nabla} \cdot \vec{A} = 0 \quad (5)$$

where \vec{j} is the electron current and the initial conditions are: $\vec{A}(t = 0) = \vec{A}_0; \varphi = 0$. The first term in the right side of Eq.(1) is the ponderomotive force [19, 27] resulting in electron evacuation whose action is compensated by the electrostatic field generated by this charge separation. In the reference frame moving with the group velocity of the laser pulse, one can consider the equilibrium conditions: $\partial N_e / \partial t = 0$, with $\frac{e}{4\gamma m \omega_L^2} \vec{\nabla}_\perp \vec{A}_0^2 = -\vec{\nabla}_\perp \varphi_0$ and equations (2), (4) and (5). Instability conditions are examined with the use of the series $F = F_0 + F_1$, where $F_1 \ll F_0$. This gives us the following set of equations:

$$mN_e^0 \frac{\partial \vec{v}_\perp}{\partial t} = -\frac{e^2}{4\pi m \omega_L^2} \left[2N_e^0 \vec{\nabla}_\perp \vec{A}_0 \vec{A}_1 - \frac{\gamma_1 N_e^0 \vec{\nabla}_\perp \vec{A}_0^2}{\gamma} \right] - eN_e^0 \vec{\nabla}_\perp \varphi_1 \quad (6)$$

$$\Delta \varphi_1 = 4\pi e N_e^1 \quad (7)$$

$$\frac{\partial N_e^1}{\partial t} = \vec{\nabla} \cdot (\vec{v}_\perp N_e^0) \quad (8)$$

$$\gamma_1 = a_0 a_1 \quad (9)$$

$$a_i = \frac{e}{m c \omega_L} \left(\frac{\partial \vec{A}_i}{c \partial t} \right) \quad (10)$$

$$\Delta \vec{A}_1 - \frac{\partial^2 \vec{A}_1}{c^2 \partial t^2} = -\frac{\partial \vec{\nabla} \varphi_1}{c^2 \partial t} + \frac{4\pi e N_e^0 \vec{v}_\perp}{c} \quad (11)$$

$$\vec{\nabla} \cdot \vec{A}_1 = 0 \quad (12)$$

Seeking a solution for $N_e^1, \varphi_1, \vec{A}_1, v_\perp$ of the following form:

$$U_1(t, r, \varphi) = \sum_m U_m(r) e^{i[\Omega t + m\varphi]}$$

where U_1 means harmonics amplitude for the functions, leads to equations mathematically equivalent to those for the Rayleigh-Taylor instability [28] even though the physical process

is completely different. A solution of equations for U_m can be found only numerically. Equations (6)-(12) are valid for a laser pulse of any arbitrary mode. However, for the instability to appear, the transverse gradient of electron density should be alternating, i.e., $\partial N_e^0/\partial r$ should change sign at least two times. Physically, this means the ponderomotive force should result not only in rarefaction but also in compression of the electron density. For a RPP and uniform plasma density this condition is sustained. The relativistic self-focusing results in both: thinning of the RPP ring and shrinking of the pulse waist that provokes electron compression near the pulse axis. By analogy with the Rayleigh-Taylor instability, the maximum increment Γ in this case can be evaluated as $\Gamma = \sqrt{\alpha/L}$ where α is the acceleration and L is the density gradient scale length or for the case: $\omega_L \Gamma = \sqrt{|\vec{\nabla}_\perp(N_e^0 a_0^2)|/4\gamma N_e^0}$. In plasma channels $\partial N_e^0/\partial r$ may approach to that for a Gaussian-like pulse with only a single change of its sign, eliminating the compression near the pulse axis. The instability, therefore, must vanish if the plasma channel is deep enough. We have to note that for Gaussian-like pulses the filamentation instability can also occur in higher density plasma [29, 30, 31], however, in these cases the source of the instability is different.

Instead of numerical analysis of approximate Eq. (6)-(12), which can give only condition(s) for the instability appearance, we perform fully relativistic particle-in-cell simulations of RPP propagation in real geometry. This allows us to study the full evolution of the pulse instability depending on laser and plasma conditions.

The fully relativistic 3D particle-in-cell (PIC) FPLaser3D code [32] employing the square weighting for currents and 'moving window' technique is used, disregarding the Kerr non-linearity. In all the simulations presented in this work the window size is $80 \mu m$ along the propagation direction and $60 \mu m \times 60 \mu m$ along the transverse direction, unless specifically mentioned. The axial resolution is $\lambda/16$ and transverse resolution is $\lambda/8$, and 8 particles per cell. The plasma length is set to 1 mm, with density gradient of length $150 \mu m$ on either edge. Calculations are performed for uniform plasma density and plasma channels. A laser pulse of wavelength 800 nm and duration of 30 fs is used for all the calculations. In order to understand the nature of the instability, the interac-

tion of RPP with different laser and plasma parameters is examined. The maximum laser intensity is varied from $I = 3 \times 10^{19}$ to $3 \times 10^{20} \text{ Wcm}^{-2}$. The uniform plasma density is also varied from $N_e = 3 \times 10^{19}$ to $3 \times 10^{20} \text{ cm}^{-3}$, and the pulse waist is varied from $w_0 = 8$ to $3 \mu\text{m}$. The plasma channels have a parabolic profile in the radial direction as $N_e(r) = N_{emin} + \Delta N_e(r^2/R_{ch}^2)$, where r is the radial coordinate, R_{ch} is the channel radius, N_{emin} is the on axis plasma density and ΔN_e is the density depth. In simulations the radius of the plasma channel is $25 \mu\text{m}$. The depth of the plasma channel is varied from 0.5 to 0.25 with respect to the maximum electron density. The focus position of the pulse is $100 \mu\text{m}$ inside the simulation box.

The initial conditions for the laser pulse transverse electric fields are found from the solutions of the parabolic equation and have the following form:

$$E_y(x, y, z) = E_0 \left[\frac{w_0}{w(x)} \right] \left[\frac{(y \cos \theta - z \sin \theta)}{w(x)} \right] \exp \left[-\frac{y^2 + z^2}{w(x)^2} \right] \exp(i\psi) \hat{y} \quad (13)$$

$$E_z(x, y, z) = E_0 \left[\frac{w_0}{w(x)} \right] \left[\frac{(z \cos \theta + y \sin \theta)}{w(x)} \right] \exp \left[-\frac{y^2 + z^2}{w(x)^2} \right] \exp(i\psi) \hat{z} \quad (14)$$

here, θ is the angle determining the polarization of the laser pulse: $\theta = 0$ corresponds to radial polarization, and $\theta = \pi/2$ to azimuthal polarization. The longitudinal component of the electric field is determined from the condition $\vec{\nabla} \cdot \vec{E} = 0$, and for a radially polarized pulse can be written as:

$$E_x(x, y, z) = E_0 \left[\frac{w_0}{w(x)} \right] \left[\frac{1}{kw(x)} \right] \left[2 \left(1 - \frac{y^2 + z^2}{w(x)^2} \right) \right] \exp \left[-\frac{y^2 + z^2}{w(x)^2} \right] \sin(\psi) + E_0 \left[\frac{w_0}{w(x)} \right] \left[\frac{1}{R_c w(x)} \right] (y^2 + z^2) \exp \left[-\frac{y^2 + z^2}{w(x)^2} \right] \cos(\psi) \hat{x} \quad (15)$$

where ψ is the optical phase given as

$$\psi = \omega_L t + kx + \frac{k(y^2 + z^2)}{2R_c} + 2 \tan^{-1} \left(\frac{x}{x_r} \right) \quad (16)$$

here, ω_L is the laser angular frequency, k is the wave number, w_0 is the beam size at the focus position, and $w(x)$ is the transverse beam size given as

$$w(x) = w_0 \sqrt{1 + \left(\frac{x}{x_r}\right)^2} \quad (17)$$

which is characterized by the Rayleigh length $x_r = \pi w_0^2/\lambda$ and R_c is the radius of curvature given as

$$R_c = x \left[1 + \left(\frac{x_r}{x}\right)^2 \right] \quad (18)$$

Following Maxwell's equations one can easily determine the corresponding magnetic field components. Fig. 1 shows the longitudinal and transverse field components of a radially polarized laser pulse. Unlike the transverse field of a linearly or circularly polarized pulse, it has a double Gaussian beam structure along transverse direction. As shown in Fig. 2, this gives a doughnut shape transverse intensity profile to the radially polarized pulse in the plane perpendicular to the propagation axis.

3 Results and discussion

At first, to check the numerical focusability of a diffraction limited radially polarized laser pulse we launch it in vacuum. The intensity of the pulse is $I = 3 \times 10^{19} \text{ Wcm}^{-2}$ and $w_0 = 8 \mu\text{m}$. The Rayleigh length of the pulse corresponding to $w_0 = 8 \mu\text{m}$ is $250 \mu\text{m}$. Fig. 2 shows the transverse intensity evolution of the pulse in vacuum. Fig. 2(a) shows transverse intensity profile of the pulse $80\mu\text{m}$ before the focus position, fig 2(b) shows transverse intensity profile at the focus position, and fig. 2(c) shows after $300 \mu\text{m}$ (1 ps) beyond the focus position. One can notice that there is no change in the transverse intensity profile of the pulse except that due to natural diffraction.

Fig. 3 shows the transverse intensity profile of the radially polarized laser pulse with exactly the same parameters as above, but now propagating in a uniform underdense

plasma of density $N_e = 3 \times 10^{19} \text{ cm}^{-3}$. One can notice from Fig. 3(b) the development of the instability after $t \approx 700 \text{ fs}$. The instability results in formation of the mode $m = 3$. This mode occurs to satisfy two kinds of symmetry : reflection and rotational symmetry. Modes $m = 1$ and $m = 2$ can not satisfy such symmetry conditions. Fig. 4 shows the corresponding transverse electron density profile. In Fig. 5 and 6 the same results are given in 3D contour plots. They confirm the separation of the RPP into three independent laser pulses. This reflects that the diffraction of the initial laser pulse prevents further development of the instability. As anticipated, an increase in intensity results in more severe instability growth. Fig. 7 shows the transverse intensity profile of the radially polarized pulse of intensity $I = 3 \times 10^{20} \text{ Wcm}^{-2}$ propagating in uniform underdense plasma of density $N_e = 3 \times 10^{19} \text{ cm}^{-3}$. In this case the instability develops faster since the acceleration increases. One can also notice from Fig. 7(d) the development of the next higher mode, $m=6$. Moreover, the diffraction of the laser pulse is weaker in this case, allowing the development of such modes. Fig. 8 shows the corresponding transverse electron density profile. Fig. 9 and 10 illustrates these results in 3D contour plots. Similar calculations for a RPP of intensity $I = 3 \times 10^{16} \text{ Wcm}^{-2}$ propagating in a uniform underdense plasma of density $N_e = 3 \times 10^{19} \text{ cm}^{-3}$ results in no instability in the first 1 ps, and then a weak sign of instability occurs. The growth rate of the instability decreases by decreasing the intensity of the pulse. Fig. 11 illustrates a weak instability development for this case. Qualitatively this confirms the dependency of the increment of the instability on acceleration as $\approx \alpha^{1/2}$.

An increase in plasma density reveals the importance of total self-focusing in the development of the filamentation instability. Fig.12 shows the transverse intensity evolution of a RPP of intensity $I = 3 \times 10^{19} \text{ Wcm}^{-2}$ propagating in uniform underdense plasma of density $N_e = 3 \times 10^{20} \text{ cm}^{-3}$. In this case the transverse window size of the simulation box is $50 \mu\text{m} \times 50 \mu\text{m}$. One can notice strong self-focusing of the RPP along with the development of the instability. Competition between the total pulse self-focusing and the thinning of the RPP ring is clearly observed. Such a non-linear process can be examined only by self-consistent particle-in-cell simulations. In Fig. 13 results of calculations for an

azimuthally polarized laser pulse of $I = 3 \times 10^{19} \text{ Wcm}^{-2}$ and $w_0 = 8 \mu\text{m}$ propagating in a uniform underdense plasma of $N_e = 3 \times 10^{19} \text{ cm}^{-3}$ are shown. The result of instability is clearly seen: the laser pulse is split into three parts. Instability increment behavior is numerically close to that for the radially polarized laser pulse. However, the resulting distribution of the intensity is not as symmetric as for the radially polarized pulse case. Again, the development of the instability is ceased by the pulse diffraction for this case also. Fig. 14 shows the corresponding transverse electron density distribution.

In order to check the effect of pulse spot size on instability development we reduced the spot of the laser pulse to $w_0 = 3 \mu\text{m}$. The intensity of the radially polarized laser pulse is $3 \times 10^{20} \text{ Wcm}^{-2}$ and plasma density is $3 \times 10^{19} \text{ cm}^{-3}$. Fig. 15 shows the transverse intensity evolution for this case. The instability development time is around 500 fs, which is less than in the case for $w_0 = 8 \mu\text{m}$ at the same intensity. This again implies the inverse dependency of the rate of instability development on density gradient scale length. Fig. 16 shows the corresponding transverse electron density evolution. These figures demonstrate a more intuitive physical behavior of transverse density modulation and instability development.

At first sight it appeared that the mode distribution is regular and is not stochastic. However, the angle at (y,z)-axis is determined in the laboratory reference frame with a rotation phase ψ_0 : $y = r \cos(\psi + \psi_0)$, $z = r \sin(\psi + \psi_0)$. Therefore, the spatial distribution of the modes may randomly vary shot-to-shot in a real experiment.

As we expected, the propagation of the RPP in parabolic plasma channels differs completely from that in uniform density plasma. In Fig. 17 and 18 transverse distribution of the pulse intensity in parabolic channels are given. In Fig. 17 the plasma channel is rather shallow $N_{emin} = 0.5N_{emax}$, while in Fig. 18 it is deeper $N_{emin} = 0.25N_{emax}$. Channel diameters are equal in both cases. One can see that after propagation of about 1.6 ps the RPP is slightly distorted in the shallow channel; in uniform density plasma this pulse would have been already split by this time of propagation. For the deeper channel there is essentially no distortion of the pulse transverse profile at all up to this time. This is attributed to the absence of electron density compression near the laser axis that removes

the source of instability.

From the above discussion it is obvious that electron acceleration in RPP wakefield in a uniform density plasma is not practical. Fig.19 shows the cross-sections of spatial distribution of electric field and electron density of RPP propagating in uniform density plasma with an intensity of $I = 3 \times 10^{19} \text{ Wcm}^{-2}$ and $w_0 = 8 \mu\text{m}$. Before splitting the wakefield is quite stochastic and cannot provide the acceleration of high quality electron beams. Moreover, after splitting the three laser pulses are propagating independently in the forward direction with gradual divergence. Such beams are hardly interesting for any practical application. In contrast, in deep plasma channel the instability vanishes and one can expect a promising scenario for the electron self-injection and their further acceleration.

In Fig.20 3D plots of density evolution for high energy component of plasma electrons are presented for RPP with $I = 3 \times 10^{20} \text{ Wcm}^{-2}$ and $w_0 = 8 \mu\text{m}$ propagating in a parabolic plasma channel of depth 0.25, i.e., $N_{emax} = 3 \times 10^{20} \text{ cm}^{-3}$ and $N_{emin} = 0.25N_{emax}$. Initially there are only plasma field oscillations in the wake, however, after 1 ps of propagation one can observe electron self-injection. Spatial distribution of trapped electrons is marked by a circle and also given as insets in Fig. 20(c). Despite the absence of the instability, the structure of laser wake field does not allow high quality beam acceleration. The energy distributions for electrons accelerated by RPP with different intensity are shown in Fig. 21. Even for high pulse intensity in uniform plasma the energy of the accelerated electrons is small, only a few tens of MeV. For the deeper channel and pulse intensity $I = 3 \times 10^{20} \text{ Wcm}^{-2}$ the maximum energy of the accelerated electrons exceeds $\gamma = 500$ in 2.2 ps. In deep plasma channel the energy distribution of the accelerated electrons display a quasi-mono-energetic feature as shown by the circle in Fig. 21(a). However, due to stochastic behavior of the injection process, the energy spectrum lost its monoenergetic feature for longer propagation time. Nevertheless, the strong axial electric field of RPP and sufficiently high energy gain of accelerated electrons in the pre-plasma channel suggests that these pulses might be useful for multistage acceleration schemes.

4 Conclusions

Using three dimensional fully relativistic particle-in-cell simulations we have investigated the filamentation instability for radially and azimuthally polarized laser pulses in uniform underdense plasma. This instability is provoked by compression of plasma electrons near the laser axis during radially or azimuthally polarized pulse self-focusing. Depending on laser intensity we have observed formation of three laser filaments for $I = 3 \times 10^{19} \text{ Wcm}^{-2}$ and six filaments for $I = 3 \times 10^{20} \text{ Wcm}^{-2}$, which afterward propagate independently. For high density plasma the filaments formation is suppressed by pulse self-focusing. The source of instability has been confirmed by disappearance of instability in the parabolic plasma channels. This implies that RPP can be guided in a spatially tailored plasma, for example using splash plasma channels [33].

Laser wake field acceleration by RPP has been explored as well. In uniform density plasma the filamentation instability makes the LWFA impractical. Divergence of laser filaments will result in poor emittance of the electron beams, if they occur. In plasma channels LWFA of electrons by RPP is more suitable. However, stochastic self-injection of plasma electrons results in poor quality electron beams. Such acceleration by conventional Gaussian pulses is much more efficient.

Acknowledgment

The authors would like to acknowledge fruitful discussions with Prof. S. V. Bulanov (JAEA) and C. Joshi (UCLA) as well as Dr. T. Inoue, and S. Ito. (Genesis Research Institute, Inc.). This work is funded by ImPACT Program of Council for Science, Technology and Innovation (Cabinet Office, Government of Japan), and partly by Genesis Research Institute, Inc.(TOYOTA Konpon-ken). This work is also supported by the Large Scale Simulation Program No. 14/15-26 (FY2015) of High Energy Accelerator Research Organization (KEK).

References

- [1] S. P. D. Mangles, C. D. Murphy, Z. Najmudin, A. G. R. Thomas, J. L. Collier, A. E. Dangor, E. J. Divall, P. S. Foster, J. G. Gallacher, C. J. Hooker, D. A. Jaroszynski, A. J. Langley, W. B. Mori, P. A. Norreys, F. S. Tsung, R. Viskup, B. R. Walton, and K. Krushelnick, *Nature*, **431**, 535 (2004); C. G. R. Geddes, C. Toth, J. V. Tilborg, E. Esarey, C. B. Schroeder, D. Bruhwiler, C. Nieter, J. Cary and W. P. Leemans, *Nature*, **431**, 538 (2004); J. Faure, Y. Glinec, A. Pukhov, S. Kiselev, S. Gordienko, E. Lefebvre, J. P. Rousseau, F. Burgy, and V. Malka, *Nature*, **431**, 541 (2004).
- [2] W. P. Leemans, B. Nagler, A. J. Gonsalves, C. Toth, K. Nakamura, C. G. R. Geddes, E. Esarey, C. B. Schroeder, and S. M. Hooker, *Nature Phys.*, **2**, 696 (2006).
- [3] T. Hosokai, K. Kinoshita, T. Ohkubo, A. Maekawa, M. Uesaka, A. Zhidkov, A. Yamazaki, H. Kotaki, M. Kando, K. Nakajima, S. V. Bulanov, P. Tomassini, A. Giulietti, and D. Giulietti, *Phys. Rev. E*, **73**, 036407 (2006).
- [4] T. Hosokai, A. Zhidkov, A. Yamazaki, M. Uesaka, and R. Kodama, *Appl. Phys. Lett.*, **96**, 121501 (2010); E. Miura, K. Koyama, S. Kato, N. Saito, M. Adachi, Y. Kawada, T. Nakamura, and M. Tanimoto, *Appl. Phys. Lett.*, **86**, 251501 (2005).
- [5] J. S. Kim, T. LaGrange, B. W. Reed, M. L. Taheri, M. R. Armstrong, W. E. King, N. D. Browning, and G. H. Campbell, *Science*, **321**, 1472 (2008).
- [6] S. Tokita, M. Hashida, S. Inoue, T. Nishoji, K. Otani, and S. Sakabe, *Phys. Rev. Lett.*, **105**, 215004 (2010).
- [7] W. Schumaker, N. Nakanii, C. McGuffey, C. Zulick, V. Chyvkov, F. Dollar, H. Habara, G. Kalintchenko, A. Maksimchuk, K. A. Tanaka, A. G. R. Thomas, V. Yanovsky, and K. Krushelnick, *Phys. Rev. Lett.*, **110**, 015003 (2013).

- [8] N. Nakanii, T. Hosokai, K. Iwasa, S. Masuda, A. Zhidkov, N. Pathak, H. Nakahara, Y. Mizuta, N. Takeguchi, and R. Kodama, *Phys. Rev. ST-AB*, **18**, 021303 (2015).
- [9] W. Leemans and E. Esarey, *Physics Today*, **62(3)**, 44 (2009).
- [10] W. Lu, M. Tzoufras, C. Joshi, F. S. Tsung, W. B. Mori, J. Vieira, R. A. Fonseca, and L. O. Silva, *Phys. Rev. ST - AB*, **10**, 061301 (2007).
- [11] A. Karmarkar and A. Pukhov, *Laser and Part. Beams*, **25**, 371 (2007).
- [12] K. P. Singh and M. Kumar, *Phys. Rev. ST-AB*, **14**, 030401 (2011).
- [13] Y. I. Salamin, *Phys. Rev. A*, **73**, 043402 (2006).
- [14] J. Vieira and J. T. Mendonca, *Phys. Rev. Lett.*, **112**, 215001 (2014).
- [15] N. Nakanii, T. Hosokai, S. Masuda, N. Pathak, A. Zhidkov, Y. Mizuta, K. Iwasa, N. Takeguchi, Z. Jin, K. Sueda, M. Mori, M. Kando, and R. Kodama, *Proceedings of Plasma Conference 2014 (PLASMA 2014)*, 18pB-2, Niigata, Japan, 2014 (<http://www.jspf.or.jp/PLASMA2014/PLACON2014/pdf/18pB-2.pdf>)
- [16] N. C. Pathak, G. Bussolino, C. A. Cecchetti, A. Giulietti, D. Giulietti, P. Koster, T. Levato, L. Labate, and L. A. Gizzi, *Nucl. Instru. Meth. Phys. Res. A*, **680**, 103 (2012).
- [17] W. L. Kruer, *The physics of laser plasma interaction* (Addison Wesley, 1988).
- [18] C. S. Liu and V. K. Tripathi, *The interaction of electromagnetic waves with electron beams and plasmas* (World Scientific).
- [19] P. Gibbon, *Short pulse laser interaction with matter* (World Scientific).
- [20] A. J. Campillo, S. L. Shapiro, and B. R. Suydam, *Appl. Phys. Lett.*, **23**, 628 (1973).

- [21] Z. K Yankauskas, *Izv. Vyssh. Uchenbn. Zaved. Radiofiz.* **9**, 261 (1966) [Sov. Radiophys. **9**, 261 (1966)].
- [22] J. M Soto-Crespo, D. R Heatley and E. M Wright, *Phys. Rev. A* **44**, 636 (1990).
- [23] D. V Skryabin and W. J Firth, *Phys. Rev. E* **58**, 1252 (1997).
- [24] C. E. Max and J. Arons, *Phys. Rev. Lett.*, **33**, 209 (1974).
- [25] N. E. Andreeva, L. M. Gorbunov, P. Mora, and R. R. Ramazashvili, *Phys. Plasmas*, **14**, 083104, (2007)
- [26] N. S. Javan and F. Adli, *Phys. Rev. E*, **88**, 043102 (2013).
- [27] B. Quesnel and P. Mora, *Phys. Rev. E*, **58**, 3719 (1998).
- [28] H. Takabe, L. Montierth, and R. L. Morse, *Phys. Fluids*, **26**, 2299 (1983).
- [29] A. Zhidkov, J. Koga, T. Hosokai, K. Kinoshita, and M. Uesaka, *Phys. Plasmas*, **11**, 5379 (2004).
- [30] N. M. Naumova, S. V. Bulanov, K. Nishihara, T. Zh. Esirkepov and F. Pegoraro, *Phys. Rev. E*, **65**, 045402 (2002).
- [31] A. Pukhov, *Rep. Prog. Phys.*, **65**, R1-R55 (2002).
- [32] A. Zhidkov, T. Fujii, and Koshichi Nemoto, *Phys. Rev. E*, **78**, 036406 (2008).
- [33] Y. Mizuta, T. Hosokai, S. Masuda, A. Zhidkov, K. Makito, N. Nakanii, S. Kajino, A. Nishida, M. Kando, M. Mori, H. Kotaki, Y. Hayashi, S. V. Bulanov and R. Kodama, *Phys. Rev. ST - AB*, **15**, 121301 (2012).

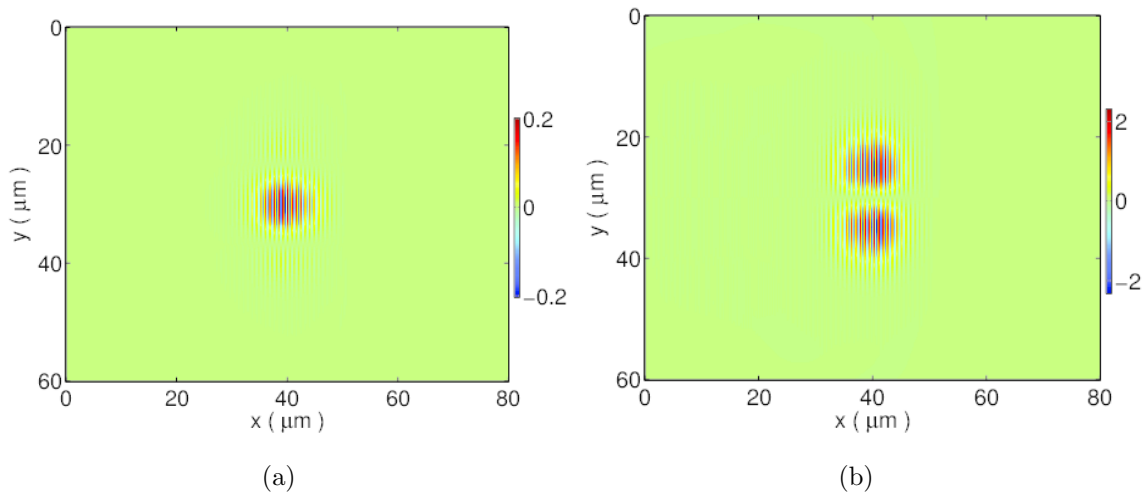


Figure 1: Snapshots of (a) axial (E_x) and (b) transverse (E_y) electric field of a 30 fs radially polarized laser pulse with intensity $3 \times 10^{19} Wcm^{-2}$ and waist size of $8\mu m$. The colorbar shows normalized laser strength parameter (a_0). The pulse is propagating from right to left hand side.

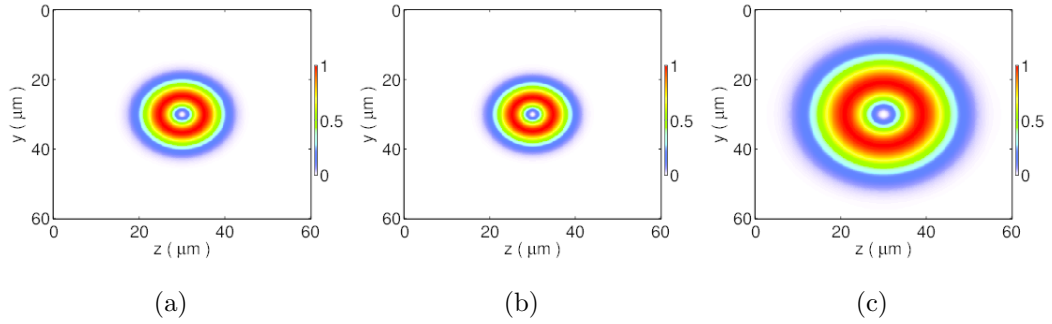


Figure 2: Transverse intensity profile of a radially polarized pulse of intensity $3 \times 10^{19} W cm^{-2}$ and $w_0 = 8 \mu m$ propagating in vacuum. The colorbar shows intensity value normalized to the maximum intensity for each figure. The Rayleigh length of the pulse corresponding to $w_0 = 8 \mu m$ is $250 \mu m$. (a) shows transverse intensity profile of the pulse $80 \mu m$ before the focus position, (b) at the focus position, and (c) after $300 \mu m$ beyond the focus position. The maximum value of a_0 corresponding to intensity distribution is (a) 2.36, (b) 2.57 and (c) 1.36. The direction of propagation is perpendicularly outward to the y-z plane.

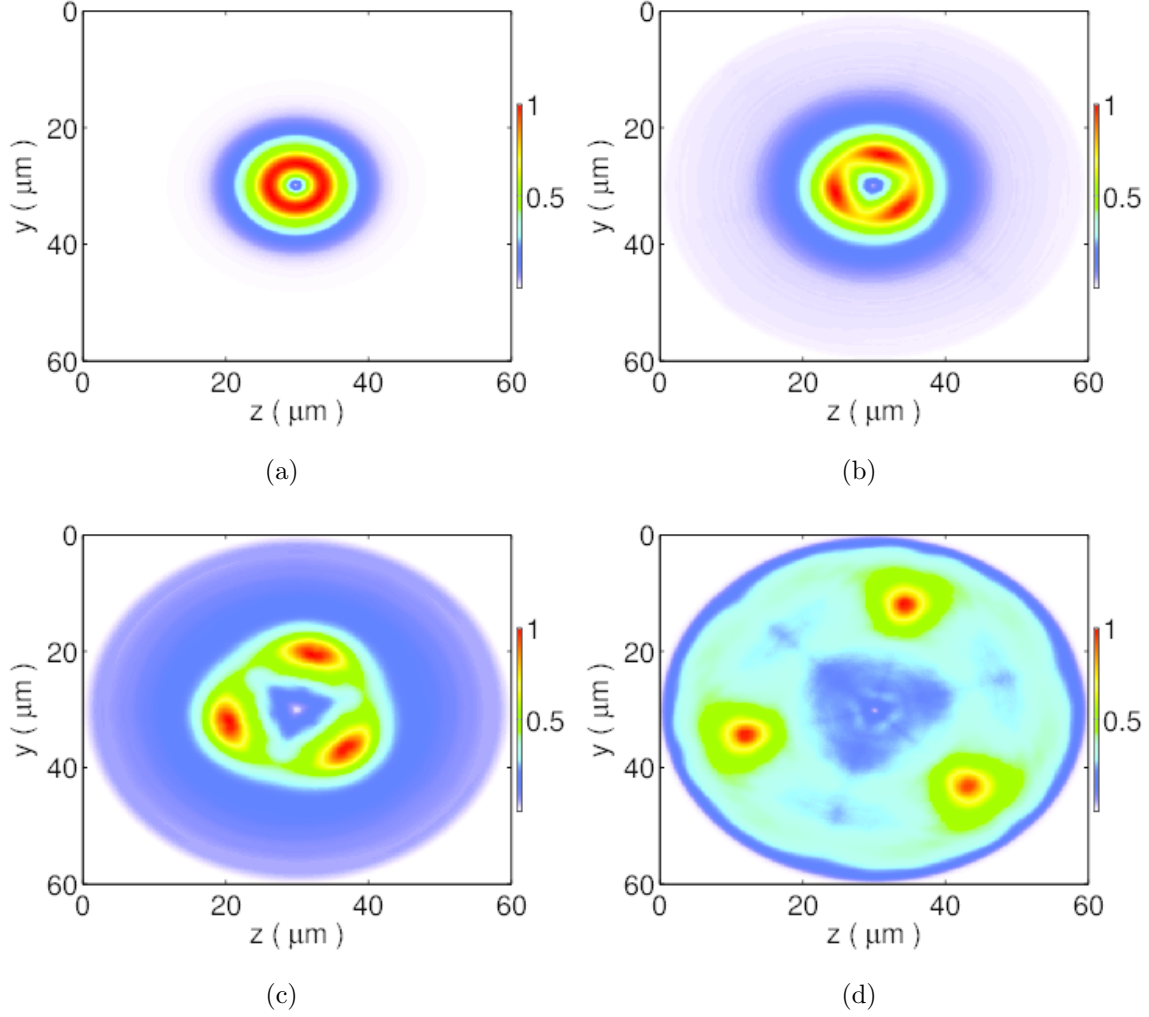


Figure 3: Transverse intensity profile of a radially polarized pulse of intensity $3 \times 10^{19} W cm^{-2}$ propagating in uniform underdense plasma of density $3 \times 10^{19} cm^{-3}$. Time corresponds to each snap shot is (a) 370 fs (b) 750 fs (c) 1.4 ps and (d) 2 ps. The colorbar shows intensity value normalized to the maximum intensity for each figure. The maximum value of a_0 corresponding to intensity distribution is (a) 1.78, (b) 2.01, (c) 1.82 and (d) 0.66. The direction of propagation is perpendicularly outward to the y-z plane.

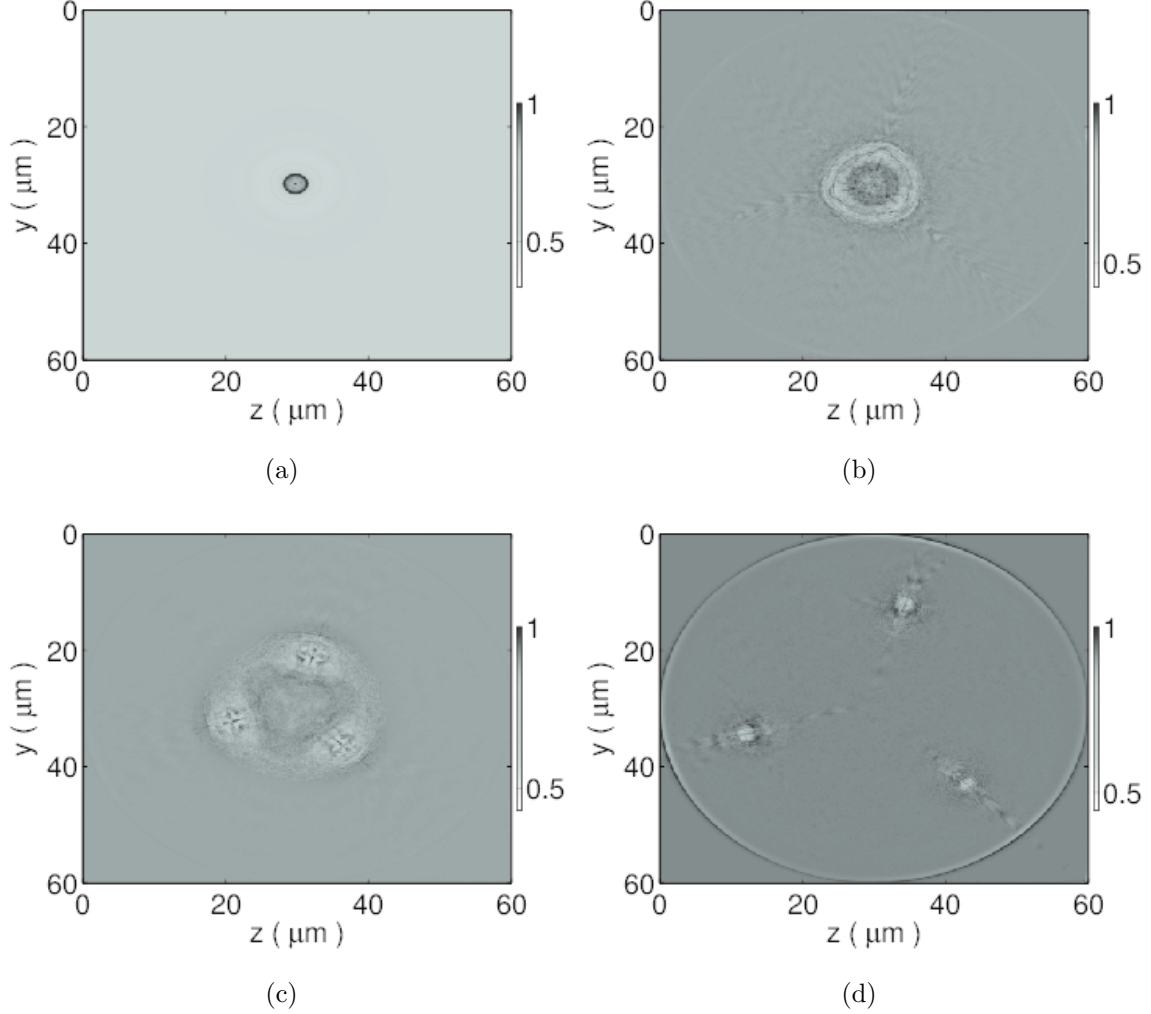


Figure 4: Transverse electron density profile of a radially polarized pulse of intensity $3 \times 10^{19} W cm^{-2}$ propagating in uniform underdense plasma of density $3 \times 10^{19} cm^{-3}$. Time corresponds to each snapshot is (a) 370 fs (b) 750 fs (c) 1.4 ps and (d) 2 ps. The gray scale bar shows density value normalized to the maximum density for each figure. The maximum value of N_e/N_c corresponding to density distribution is (a) 0.07, (b) 0.20, (c) 0.61 and (d) 0.05. The direction of propagation is perpendicularly outward to the y-z plane.

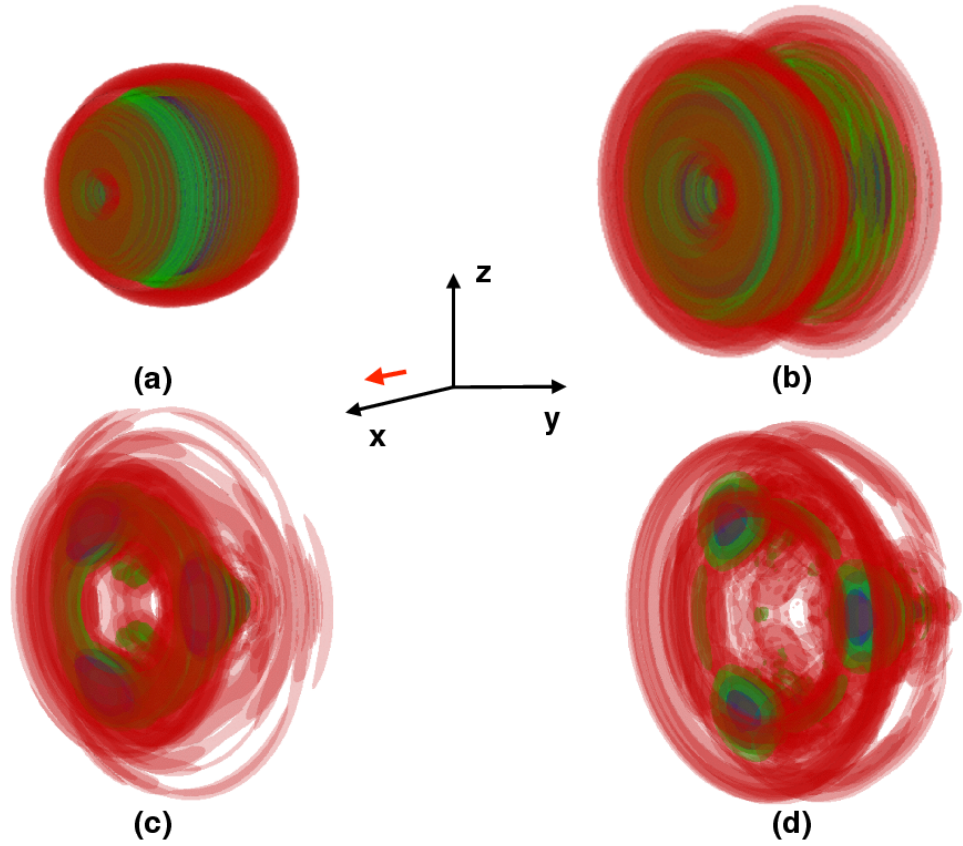


Figure 5: 3-D contour plots of intensity evolution of a radially polarized pulse of intensity $3 \times 10^{19} W cm^{-2}$ propagating in uniform underdense plasma of density $3 \times 10^{19} cm^{-3}$. The snap shots show intensity distribution at (a) 370 fs, (b) 750 fs, (c) 1.4 ps, and (d) 2 ps. The x, y, z triad corresponds to the Cartesian coordinates of the simulation geometry and arrow indicates the direction of propagation of the pulse.

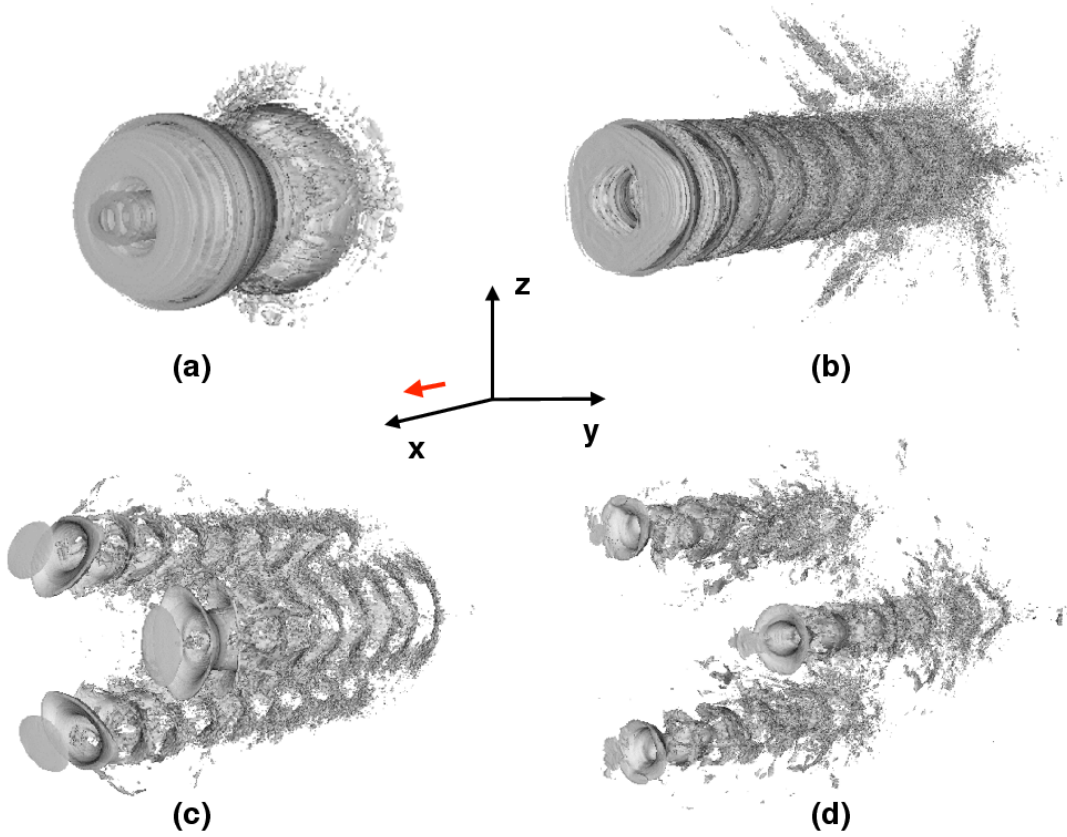


Figure 6: 3-D contour plots of electron density evolution of a radially polarized pulse of intensity $3 \times 10^{19} W cm^{-2}$ propagating in uniform underdense plasma of density $3 \times 10^{19} cm^{-3}$. The snap shots show density distribution at (a) 370 fs, (b) 750 fs, (c) 1.4 ps, and (d) 2 ps. The x, y, z triad corresponds to the Cartesian coordinates of the simulation geometry and arrow indicates the direction of propagation of the pulse.

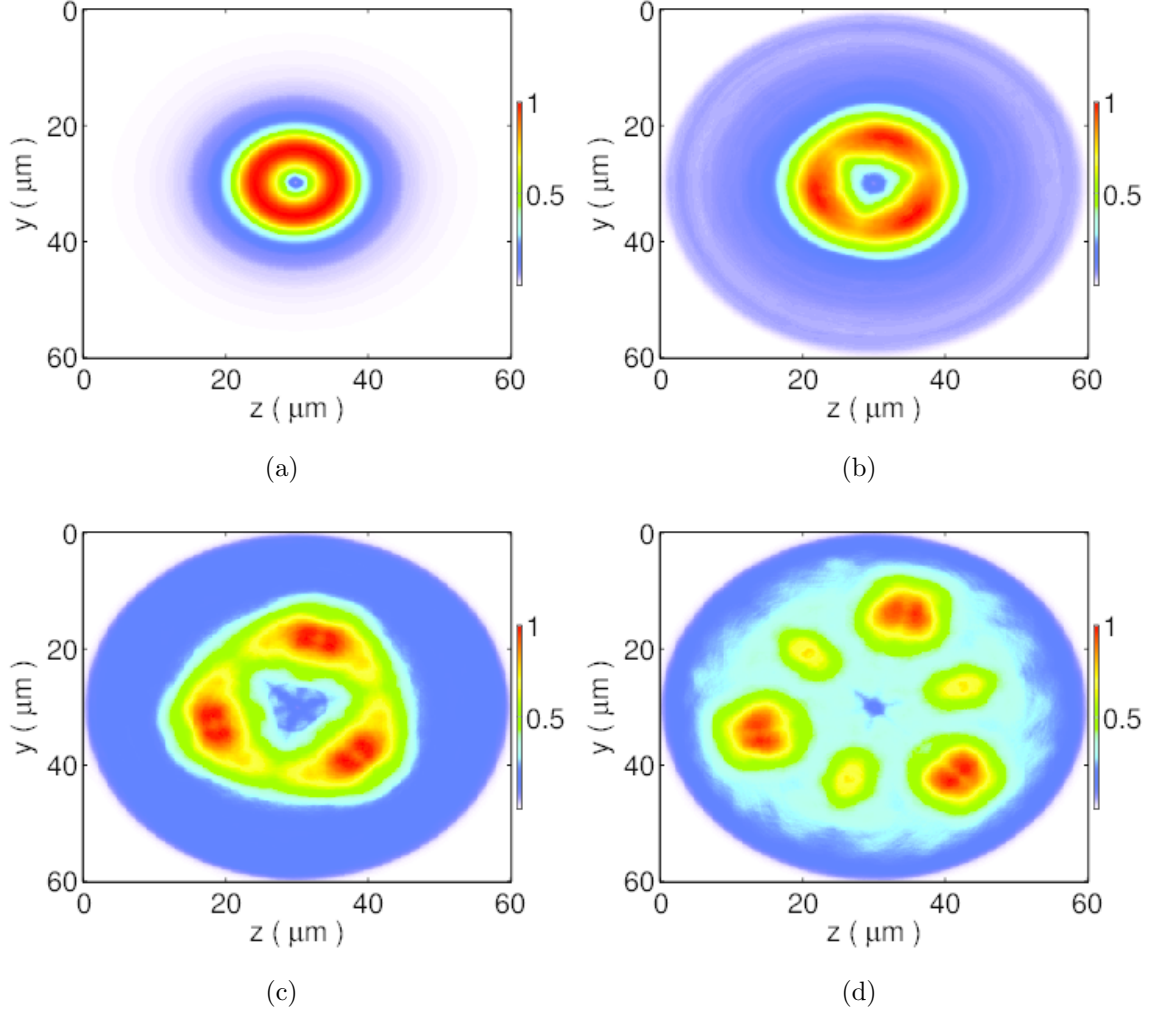


Figure 7: Transverse intensity profile of a radially polarized pulse of intensity $3 \times 10^{20} W cm^{-2}$ propagating in uniform underdense plasma of density $3 \times 10^{19} cm^{-3}$. Time corresponds to each snap shot is (a) 384 fs (b) 845 fs (c) 1.3 ps and (d) 1.8 ps. The colorbar shows intensity value normalized to the maximum intensity for each figure. The maximum value of a_0 corresponding to intensity distribution is (a) 5.62, (b) 4.53, (c) 4.31 and (d) 2.02. The direction of propagation is perpendicularly outward to the y-z plane.

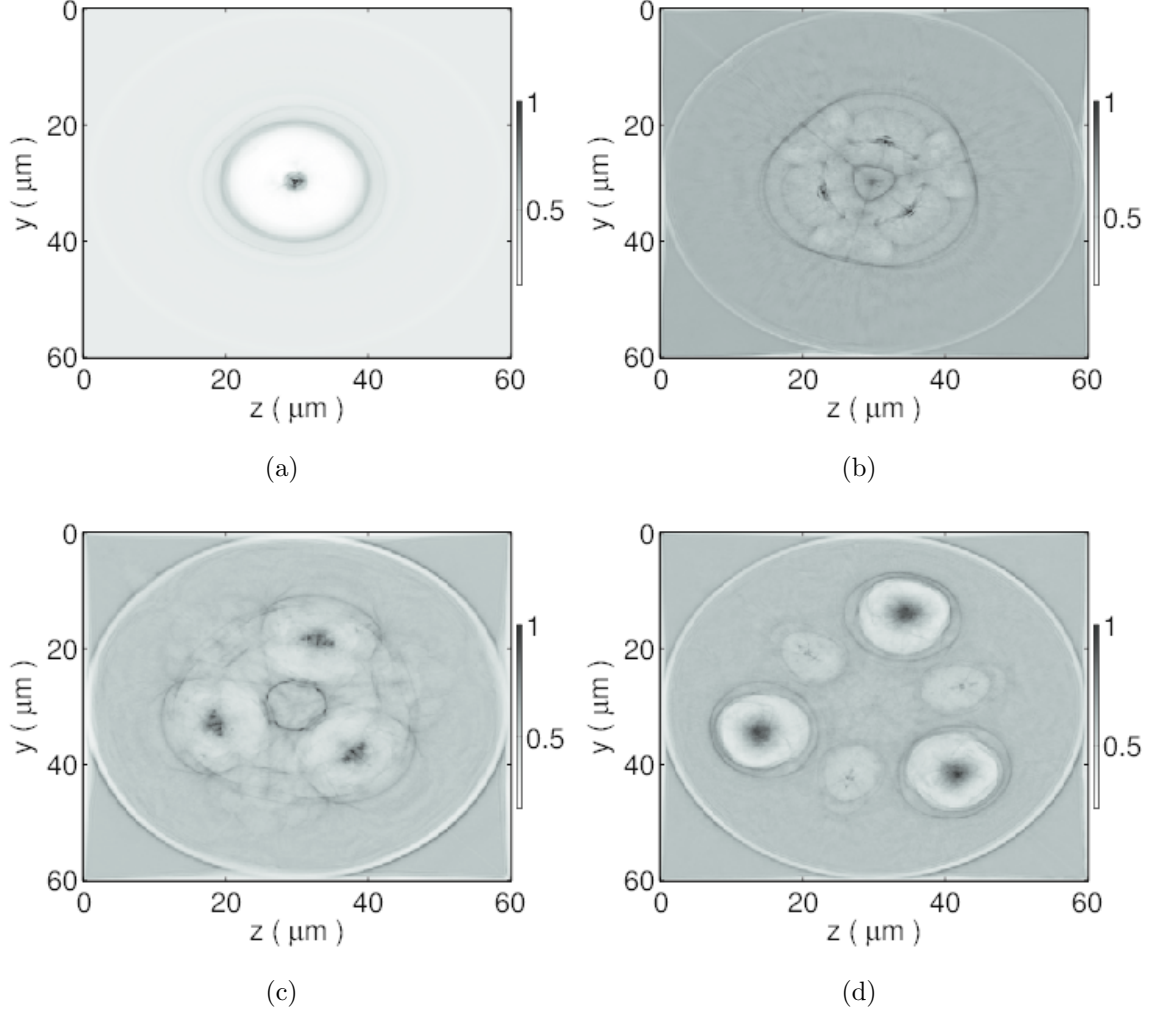


Figure 8: Transverse electron density profile of a radially polarized pulse of intensity $3 \times 10^{20} W cm^{-2}$ propagating in uniform underdense plasma of density $3 \times 10^{19} cm^{-3}$. Time corresponds to each snap shot is (a) 384 fs (b) 845 fs (c) 1.3 ps and (d) 1.8 ps. The gray scale bar shows density value normalized to the maximum density for each figure. The maximum value of N_e/N_c corresponding to density distribution is (a) 0.13, (b) 2.57, (c) 0.64 and (d) 0.24. The direction of propagation is perpendicularly outward to the y-z plane.

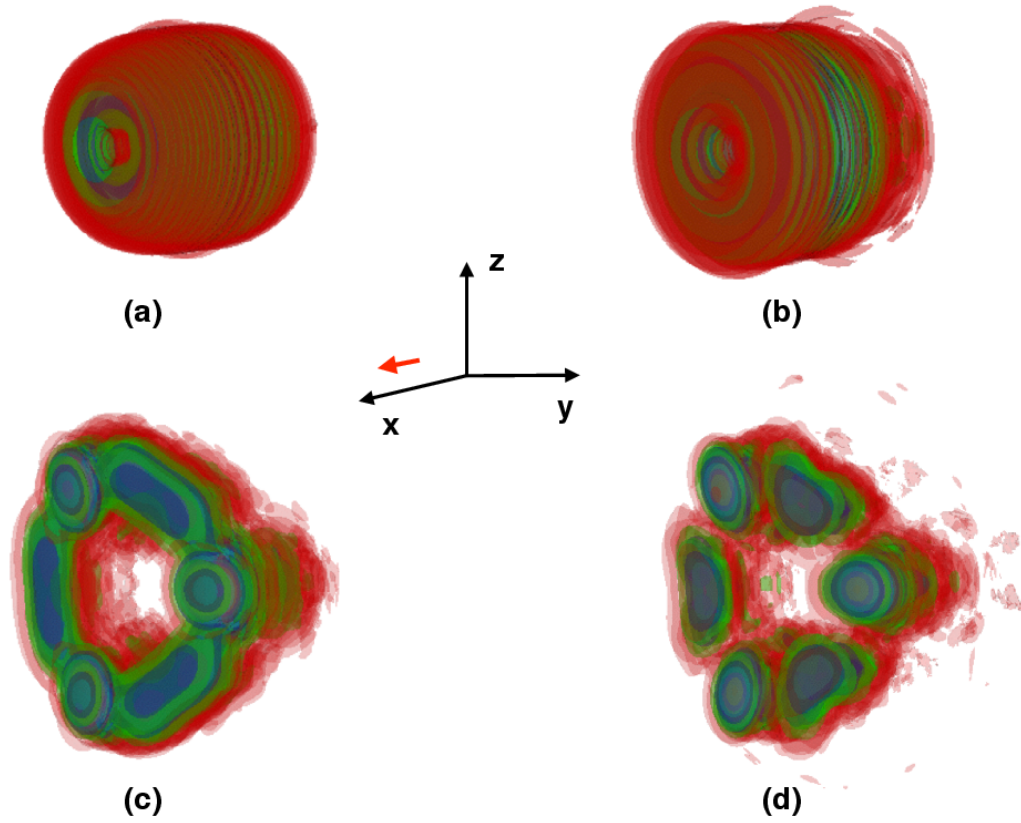


Figure 9: 3-D contour plots of intensity evolution of a radially polarized pulse of intensity $3 \times 10^{20} W cm^{-2}$ propagating in uniform underdense plasma of density $3 \times 10^{19} cm^{-3}$. The snap shots show intensity distribution at (a) 384 fs, (b) 845 fs, (c) 1.3 ps, and (d) 1.8 ps. The x, y, z triad corresponds to the Cartesian coordinates of the simulation geometry and arrow indicates the direction of propagation of the pulse.

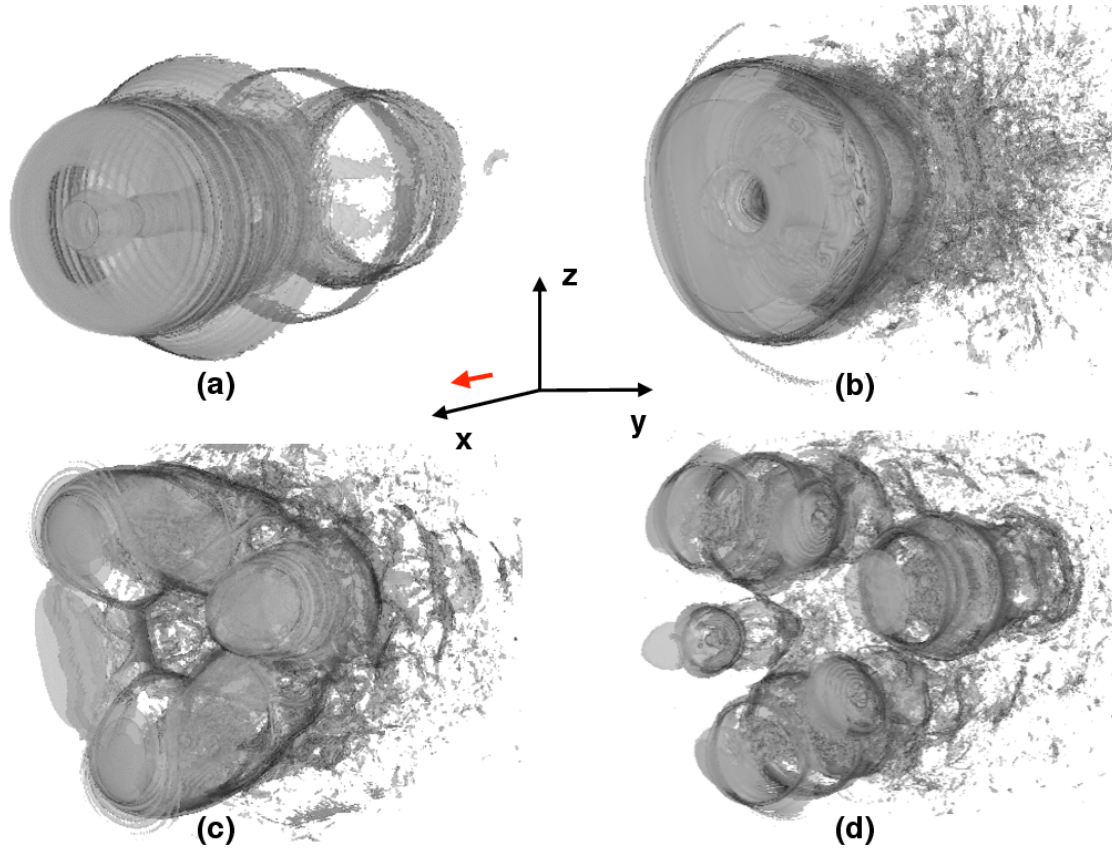


Figure 10: 3-D contour plots of electron density evolution of a radially polarized pulse of intensity $3 \times 10^{20} W cm^{-2}$ propagating in uniform underdense plasma of density $3 \times 10^{19} cm^{-3}$. The snap shots show density distribution at (a) 384 fs, (b) 845 fs, (c) 1.3 ps, and (d) 1.8 ps. The x, y, z triad corresponds to the Cartesian coordinates of the simulation geometry and arrow indicates the direction of propagation of the pulse.

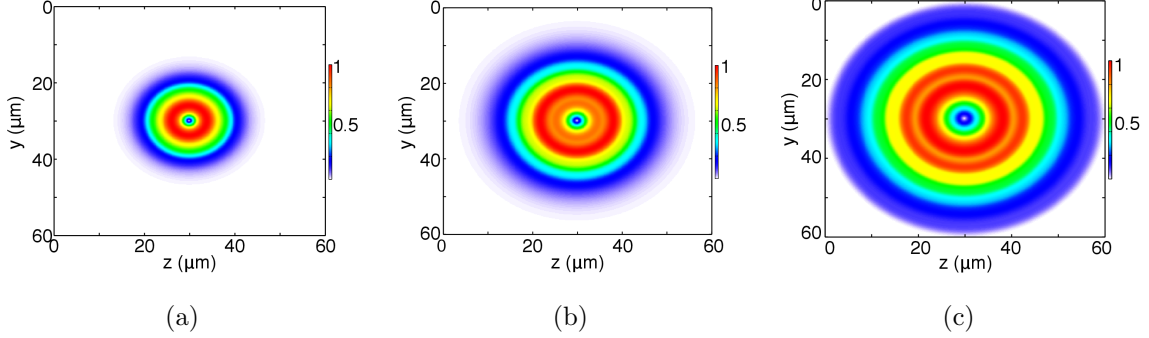


Figure 11: Transverse intensity profile of a radially polarized pulse of intensity $3 \times 10^{16} W cm^{-2}$ propagating in uniform underdense plasma of density $3 \times 10^{19} cm^{-3}$. Time corresponds to each snap shot is (a) 555 fs (b) 774 fs and (c) 1 ps. The colorbar shows intensity value normalized to the maximum intensity for each figure. The direction of propagation is perpendicularly outward to the y-z plane.

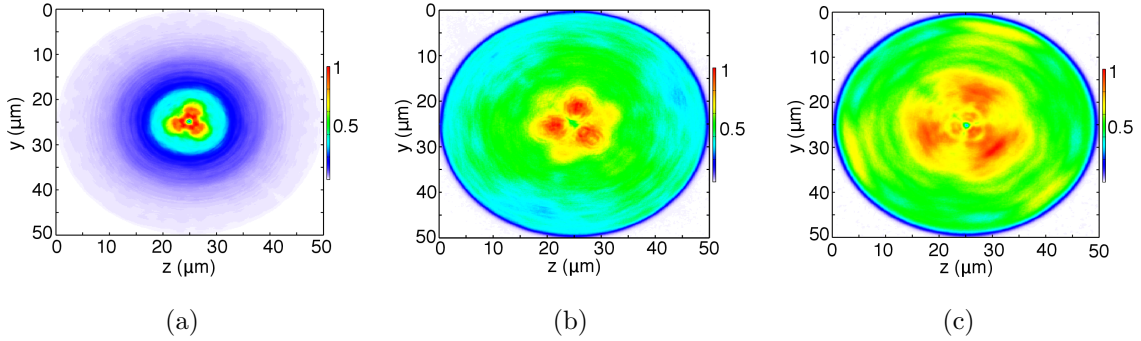


Figure 12: Transverse intensity profile of a radially polarized pulse of intensity $3 \times 10^{20} W cm^{-2}$ propagating in uniform underdense plasma of density $3 \times 10^{20} cm^{-3}$. Time corresponds to each snap shot is (a) 359 fs (b) 719 fs and (c) 1.2 ps. The colorbar shows intensity value normalized to the maximum intensity for each figure. The maximum value of a_0 corresponding to intensity distribution is (a) 3.26, (b) 0.31 and (c) 0.15. The direction of propagation is perpendicularly outward to the y-z plane.

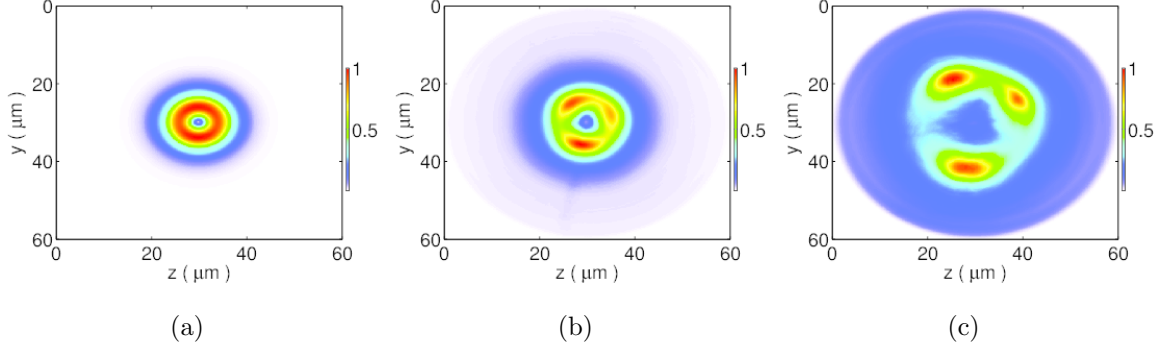


Figure 13: Transverse intensity profile of an azimuthally polarized pulse of intensity $3 \times 10^{19} W cm^{-2}$ propagating in uniform underdense plasma of density $3 \times 10^{19} cm^{-3}$. Time corresponds to each snap shot is (a) 362 fs (b) 773 fs and (c) 1.3 ps. The colorbar shows intensity value normalized to the maximum intensity for each figure. The maximum value of a_0 corresponding to intensity distribution is (a) 1.28, (b) 0.74 and (c) 0.22. The direction of propagation is perpendicularly outward to the y-z plane.

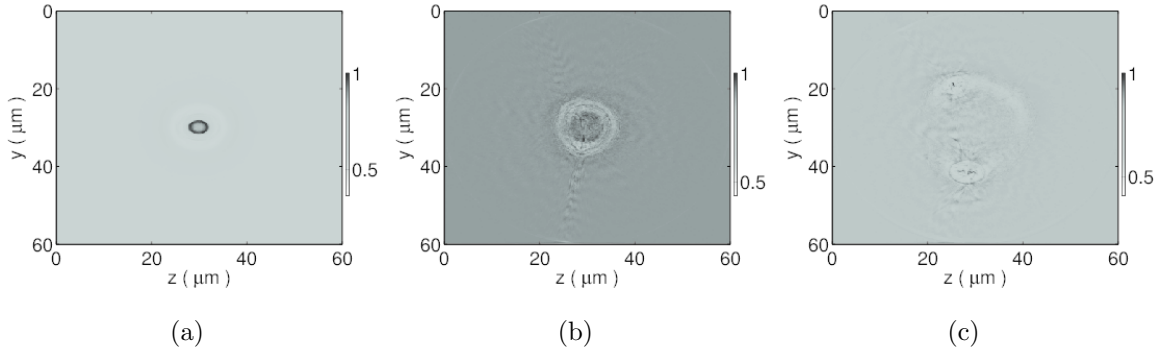


Figure 14: Transverse electron density profile of an azimuthally polarized pulse of intensity $3 \times 10^{19} W cm^{-2}$ propagating in uniform underdense plasma of density $3 \times 10^{19} cm^{-3}$. Time corresponds to each snap shot is (a) 362 fs (b) 773 fs and (c) 1.3 ps. The gray scale bar shows density value normalized to the maximum density for each figure. The maximum value of N_e/N_c corresponding to density distribution is (a) 0.06, (b) 0.09 and (c) 0.05. The direction of propagation is perpendicularly outward to the y-z plane.

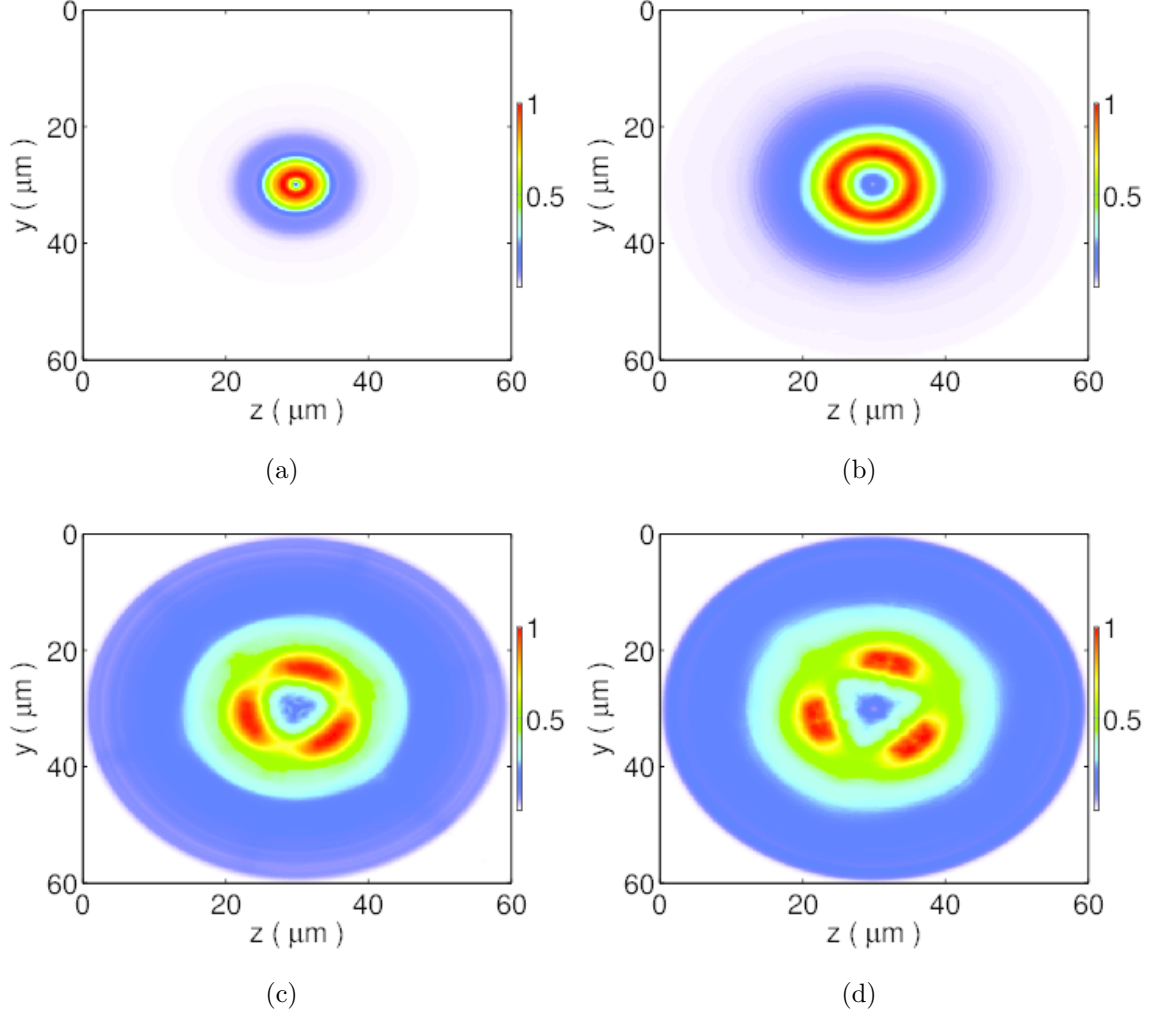


Figure 15: Transverse intensity profile of a radially polarized pulse of intensity $3 \times 10^{20} Wcm^{-2}$ and $w_0 = 3\mu m$ propagating in uniform underdense plasma of density $3 \times 10^{19} cm^{-3}$. Time corresponds to each snap shot is (a) 322 fs (b) 543 fs (c) 780 fs and (d) 900 fs. The colorbar shows intensity value normalized to the maximum intensity for each figure. The maximum value of a_0 corresponding to intensity distribution is (a) 4.44, (b) 3.58, (c) 3.64 and (d) 3.04. The direction of propagation is perpendicularly outward to the y - z plane.

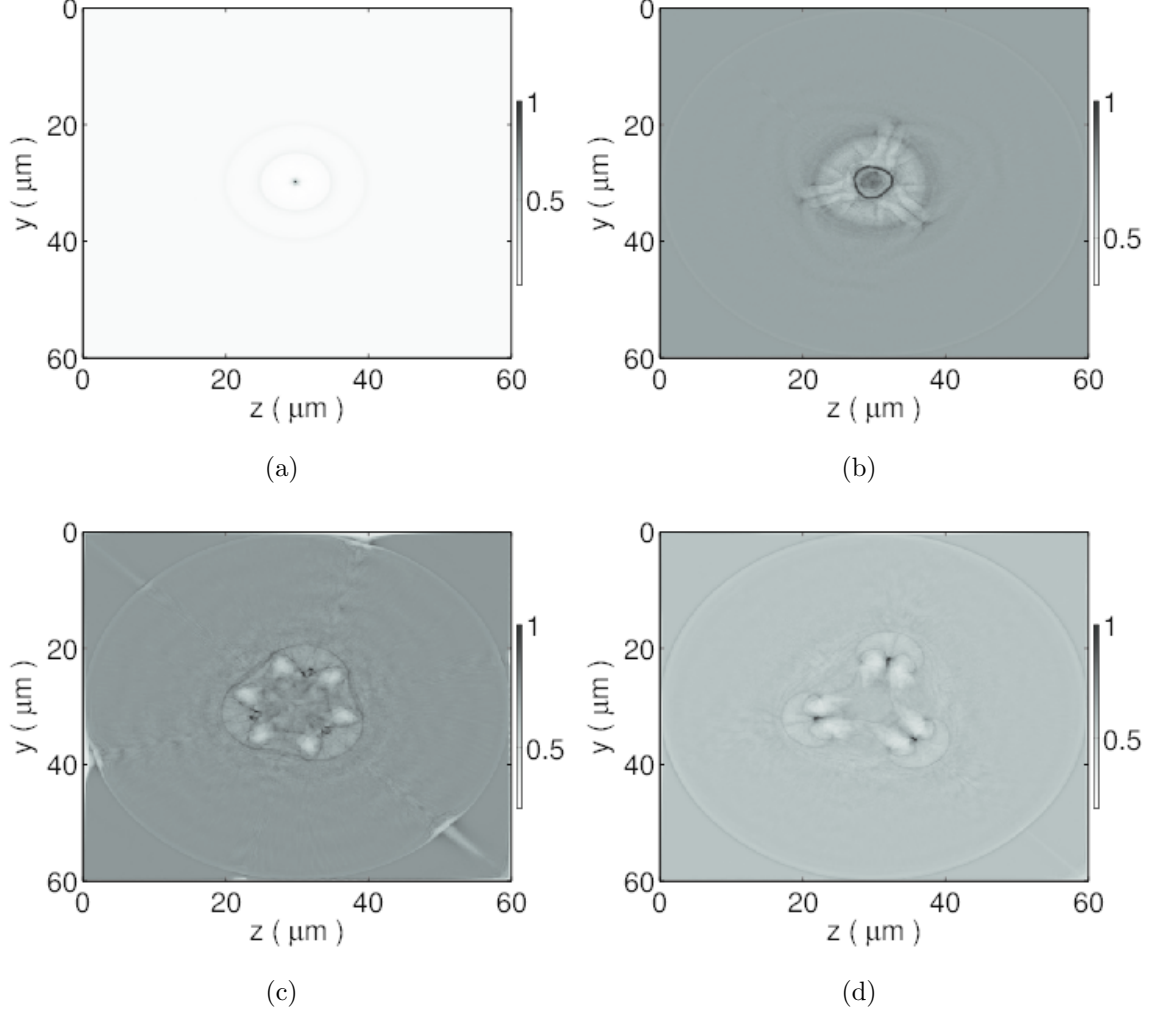


Figure 16: Transverse electron density profile of a radially polarized pulse of intensity $3 \times 10^{20} Wcm^{-2}$ and $w_0 = 3\mu m$ propagating in uniform underdense plasma of density $3 \times 10^{19} cm^{-3}$. Time corresponds to each snap shot is (a) 322 fs (b) 543 fs (c) 780 fs and (d) 900 fs. The gray scale bar shows density value normalized to the maximum density for each figure. The maximum value of N_e/N_c corresponding to density distribution is (a) 0.1287, (b) 0.21, (c) 1.47 and (d) 1.65. The direction of propagation is perpendicularly outward to the y-z plane.

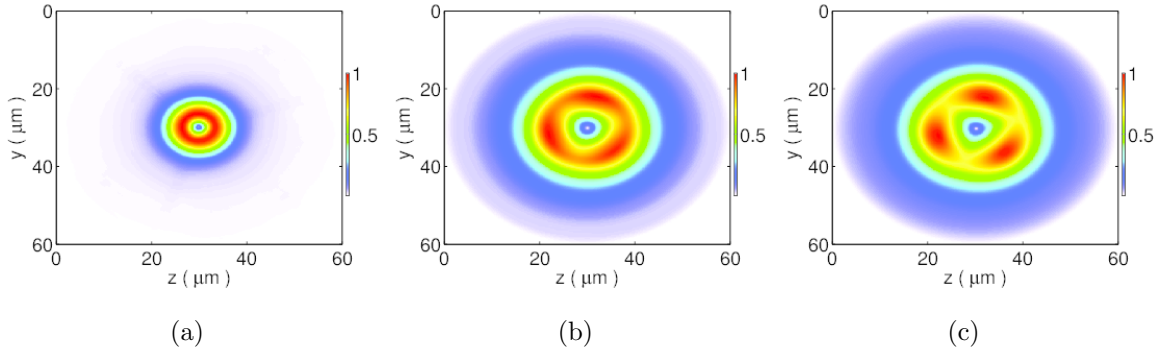


Figure 17: Transverse intensity profile of a radially polarized pulse of intensity $3 \times 10^{19} Wcm^{-2}$ propagating in underdense plasma with parabolic density profile of depth 0.5 ($N_{emax} = 3 \times 10^{19}$ and $N_{emin} = 0.5N_{emax}$). Time corresponds to each snap shot is (a) 544 fs (b) 1 ps and (c) 1.6 ps. The colorbar shows intensity value normalized to the maximum intensity for each figure. The maximum value of a_0 corresponding to intensity distribution is (a) 2.13, (b) 1.19 and (c) 1.18. The direction of propagation is perpendicularly outward to the y-z plane.

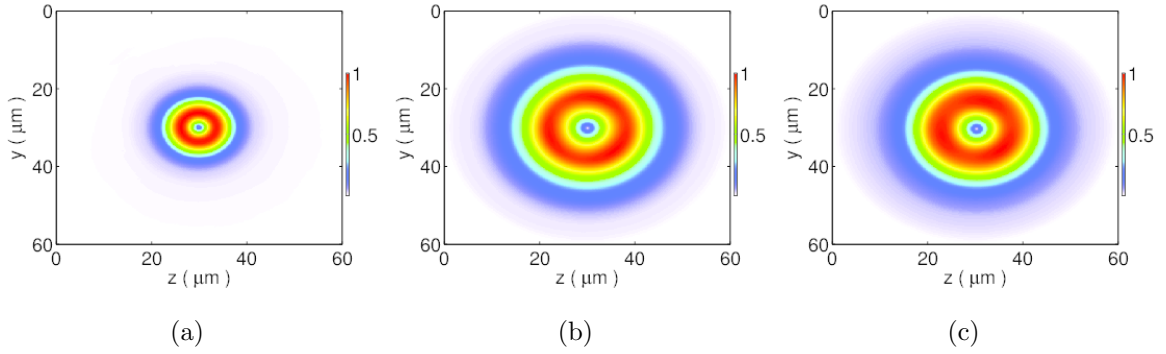


Figure 18: Transverse intensity profile of a radially polarized pulse of intensity $3 \times 10^{19} W cm^{-2}$ propagating in underdense plasma with parabolic density profile of depth 0.25 ($N_{emax} = 3 \times 10^{19}$ and $N_{emin} = 0.25N_{emax}$). Time corresponds to each snap shot is (a) 544 fs (b) 1 ps and (c) 1.6 ps. The colorbar shows intensity value normalized to the maximum intensity for each figure. The maximum value of a_0 corresponding to intensity distribution is (a) 2.07, (b) 1.04 and (c) 1.12. The direction of propagation is perpendicularly outward to the y-z plane.

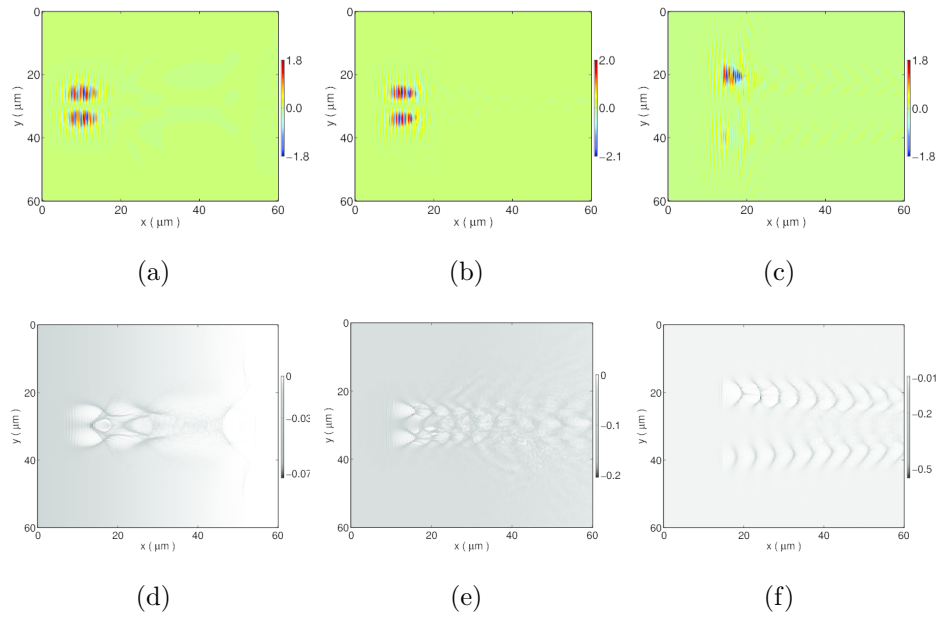


Figure 19: Transverse electric field (E_y) evolution (a,b,c) of a radially polarized pulse of intensity $3 \times 10^{19} \text{W cm}^{-2}$ propagating in uniform underdense plasma of density $3 \times 10^{19} \text{cm}^{-3}$. Panel (d,e,f) are the corresponding electron density evolution. The direction of propagation of the pulse is from right to left hand side.

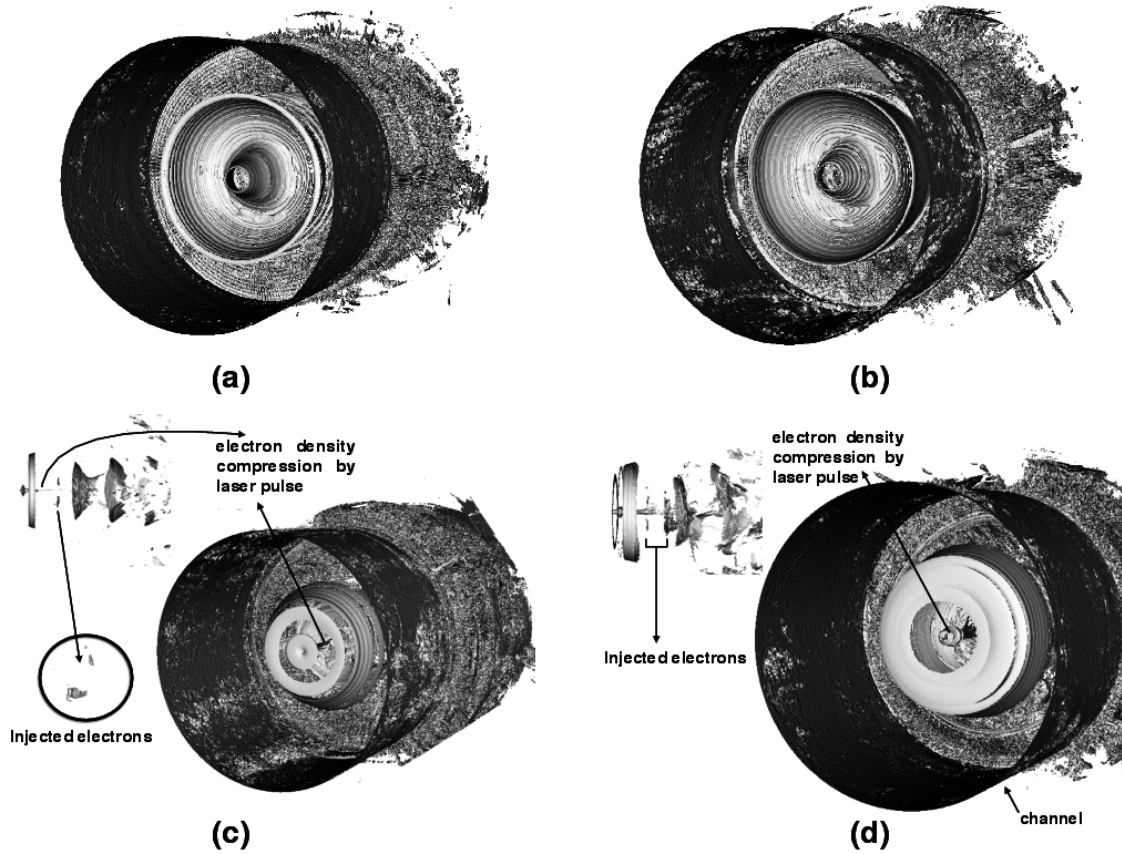


Figure 20: 3-D contour plots of electron density evolution of a radially polarized pulse of intensity $3 \times 10^{20} W cm^{-2}$ propagating in underdense plasma with parabolic density profile of depth 0.25 ($N_{emax} = 3 \times 10^{20}$ and $N_{emin} = 0.25N_{emax}$). The snap shots show density distribution at (a) 492 fs, (b,) 1.2 ps, (c) 1.8 ps and (d) 2.2 ps.

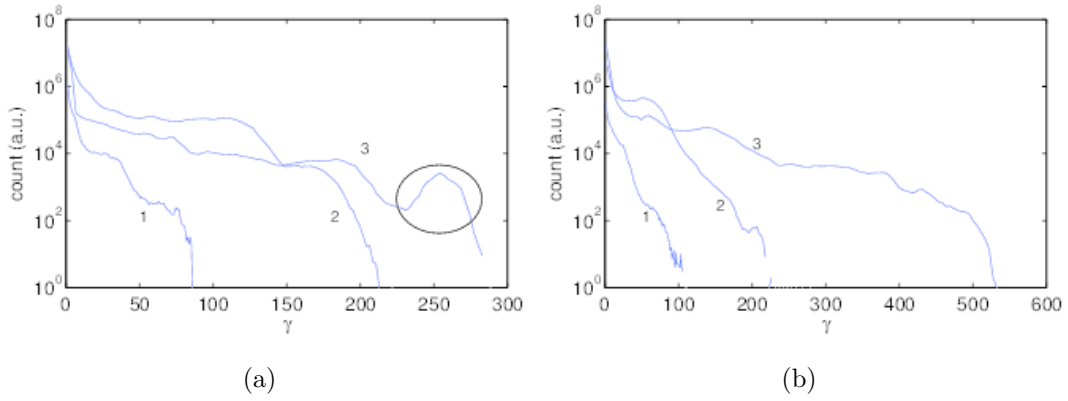


Figure 21: Energy spectrum of electrons accelerated by a radially polarized pulse of varying intensity and propagating in different plasma conditions: (1) $I = 3 \times 10^{19} Wcm^{-2}$ and uniform plasma density of $3 \times 10^{19} cm^{-3}$, (2) $I = 3 \times 10^{20} Wcm^{-2}$ and uniform plasma density of $N_e = 3 \times 10^{19} cm^{-3}$, and (3) $I = 3 \times 10^{20} Wcm^{-2}$ and parabolic plasma channel of depth 0.25 and maximum density $N_{emax} = 3 \times 10^{20} cm^{-3}$. The circle shows monoenergetic electron beam signature in plasma channel. The figure shows energy spectrum after (a) 1.4 ps and (b) 2.2 ps of propagation.